

Aerodynamic and External Ballistic Modelling of a Rocket Target with Two Motors in a Parallel Configuration

Hari Prasanna MANIMARAN*, **Algimantas FEDARAVIČIUS****

**Department of Transport Engineering, Kaunas University of Technology, K. Donelaičio st.73, LT-44249, Kaunas, Lithuania, E-mail: hari.manimaran@ktu.edu*

***Department of Mechanical Engineering, Kaunas University of Technology, K. Donelaičio st.73, LT-44249, Kaunas, Lithuania, E-mail: algimantas.fedaravicius@ktu.lt*

<https://doi.org/10.5755/j02.mech.32140>

1. Introduction

RT-400 is the short-range rocket target used for live fire exercises. RT-400 uses one RM-12K motor for propulsion. RT-400 denotes a rocket target with a 400 mm diameter body and RM 12K stands for rocket motor with 12 kN thrust. This motor was designed and developed by a group of researchers at the Kaunas University of Technology and can boost the rocket to travel up to 5 km in range. It is used as an ariel target for the short-range air defence system. This rocket is used to practice in a simulated battlefield environment to imitate real rockets or aircraft and act as a target to improve personnel skills. The demand for upgrading this rocket to increase the range for medium-range air defence systems with a maximum of 20 km leads to the research on a new variant of rocket target with extended thrust. The total thrust of the rocket can be increased by adding a new motor with improved propellant or adding more propellant. But this will lead to a requirement for research and development on the new motor and add additional overall product cost. The proposal of adding four motors in a parallel configuration and firing all four motors together or using two motors in the first stage and another two motors in the second stage is being considered. As part of the research, it is essential to numerically analyse the two possibilities before the experimental test. This method eliminates the need for a single rocket motor with increased thrust. This method of stacking four motors will satisfy the demand for cost-effective rocket targets. In this research only the first variant with two motors will be analysed and based on the results four and two-stage rockets will be considered for analysis. RT-400 was tested only with one motor. So, it is essential to do research with multiple motors to study their performance.

Aerodynamics and stability are important aspects of the rocket's external ballistics. In this research, only the aerodynamics of the rocket in subsonic speed and its influence on the external ballistics is studied. The shape of the frontal nose of the rocket is essential for aerodynamic performance at various speed regimes [1]. The geometry of the rocket target and external ballistics needs to be analysed and optimised for efficient design [2]. The study of aerodynamics is essential to predict the drag force based on the external shape [3]. The range and maximum altitude to be reached at different launch angles are based on the velocity of the rocket. The velocity and acceleration variation of the rocket for various stages of the flight also need to be calculated.

Theoretical, computational, and experimental analyzes are all possible methodologies used to study the aerodynamics of the rocket body [4]. Compared to experimental investigations, computational design and analysis provide economic benefits. The computational model will be used for the preliminary analysis [5]. The design can be changed computationally according to the findings. The numerical results will be used to create the prototype.

The objective of this research is to perform an aerodynamic analysis of various nose geometry shapes to select a lower-drag model for a rocket target and to use the final model to perform a ballistic analysis of the two-motor variant of the rocket target RT-400M.

2. Nose cone design

The shape of the nose cone contributes to the variation in drag and flow characteristics. The reduction of drag that leads to the decrement of the drag coefficient is essential for the improvement of a rocket or any aerodynamic body [6]. For a different flow regime and fluid domain, the shape of the nose produces different drag values. This value must be calculated and analysed for the aerodynamic body at the subsonic speed [7]. Pressure drag, skin friction drags, and wave drag are faced by the nose cone at this speed regime. The shape of the geometry contributes to the pressure drag as the high-concentration fluid stagnates at the tip of the nose and low pressure at the rear end of the body. The flow of fluid over the rigid body causes friction between the fluid layer and the body, causing skin friction drag[8]. Wave drag occurs mainly in the supersonic regime due to the formation of the shock wave [9]. The body tube is subjected to mostly skin friction drag and less pressure drag. As this research is mostly focused on the nose shape of the rocket, drag on the body tube is not researched in detail. Separation of the boundary layer should be delayed, and the flow must be attached to the body is preferred.

The design of the rocket body is done using the SolidWorks Student Premium with geometry correction and watertight closed geometry preferred for computational fluid analysis. The rocket body of RT-400M has a length of 5.4 meters with a diameter of 0.41 m and an overall diameter including fins of 1.3 m. The overall mass was 198.05 kg. The rocket's cross-sectional area of 0.132 m². The fin is placed at the rear end of the rocket with a trapezoidal shape in a clipped delta configuration. The nose cone of various shapes is designed for analysis. Most used nose shapes are elliptical, parabolic, ogive, conical, and blunted nose shapes [10].

The following formulas and equations are used to design the nose cone shape.

A conic section is common and easy to manufacture. It has an edge-tipped conic shape mostly preferred for supersonic speed regimes.

$$y = \frac{R}{L}x, \quad (1)$$

$$\phi = \arctan\left(\frac{R}{L}\right), \quad (2)$$

where: y is the radius at any point x ; R is the radius of the base; L is the overall length; x is the longitudinal axis; ϕ is the half angle.

The tangent ogive is a simple conical shape that forms from the segment of the circle and the curve is tangent to the body tube.

$$\rho = \frac{R^2 + L^2}{2R}, \quad (3)$$

$$y = \sqrt{\rho^2 - (L-x)^2} + R - \rho, \quad (4)$$

where: ρ is the ogive radius.

The spherically blunted conic is shaped with a nose blunted from the ogive shape. The blunted nose is of a semicircle shape.

$$x_0 = L - \sqrt{(\rho - r_n)^2 - (\rho - R)^2}, \quad (5)$$

$$y_i = \frac{r_n(\rho - R)}{\rho - r_n}; x_i = x_0 - \sqrt{r_n^2 - y_i^2}, \quad (6)$$

where: r_n is the radius of the shape; x_0 is the centre of the semicircle to the tip of the cone.

Bi-conic is shaped by placing a cone on the conical transition section.

$$L = L_1 + L_2, \quad (7)$$

$$\phi_1 = \arctan\left(\frac{R_1}{L_1}\right); \phi_2 = \arctan\left(\frac{R_2 - R_1}{L_2}\right), \quad (8)$$

$$y = x \cdot \arctan \phi_1, \quad (9)$$

$$y = R_1 + (x - L_1) \tan \phi_2, \quad (10)$$

where: L_1 is the length of the cone; L_2 is the length of the frustum; ϕ_1 is the angle of the cone; ϕ_2 is the angle of the frustum.

The parabolic shape obtained from the rotation of the parabola with the k' value varies from 0 to 1.

$$y = R \left[\frac{2\frac{x}{L} - k' \left(\frac{x}{L}\right)^2}{2 - k'} \right]. \quad (11)$$

The elliptical shape is obtained from the rotation of half of the ellipse about its major axis. This is mostly preferred for subsonic-speed projectiles.

$$y = R \sqrt{1 - \frac{(x)^2}{L^2}}. \quad (12)$$

Fig. 1 shows the six selected nose cone geometries for the rocket target RT-400M.

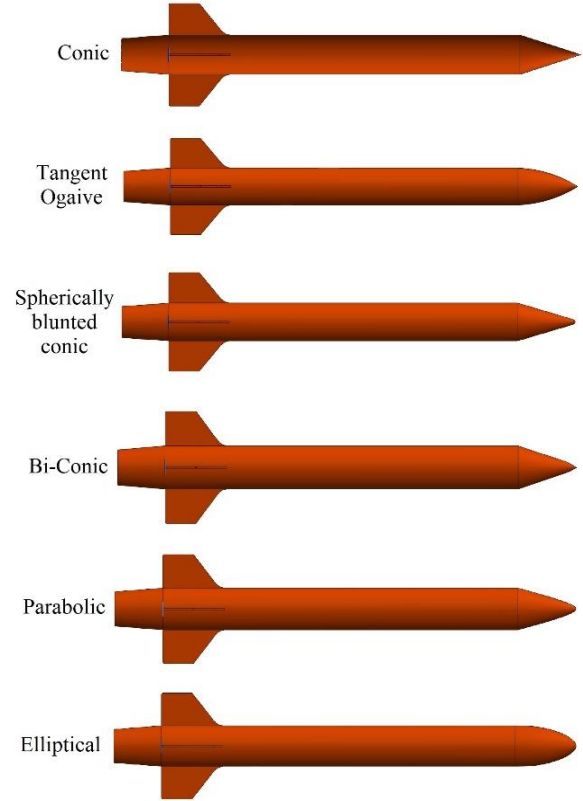


Fig. 1 Rocket target with different nose cone

3. Rocket target aerodynamic modelling

A numerical simulation of the fluid flow around the rocket body is generated using the ANSYS Fluent software package. The CFD code is used to analyse the effect of the fluid on the rigid body and the production of drag [11]. The SolidWorks model is imported to the fluent workbench for the CFD analysis. The cylindrical fluid domain is created around the rocket body with a front upstream distance of three times the length of the rocket and downstream of seven times the length of the rocket and a far-field distance of three times the diameter of the rocket. As the rocket body is axially symmetric, the domain is cut symmetrically. Then the face is computed as a symmetry boundary condition to reduce the computational time.

A hybrid mesh type of both hexahedral and tetrahedral mesh is chosen. Near the boundary with the inflation layer, the hexahedral mesh is used in the fluid region [12]. A high concentration of unstructured tetrahedral mesh is applied near the rocket body to study the flow behaviour accurately. Fairfield is made with lesser dense mesh. The maximum size of the mesh with 10 cm with 10 inflation layers with a maximum thickness of 10 cm and with a growth rate

of 1.2 is applied. A total of 13 million elements were created, as shown in Fig. 2 with high smoothing and curvature adaptation. Maximum skewness of 0.97 and minimum aspect ratio of 1.15 are obtained. The frontal face of the domain is named an inlet and the rear end face is named an outlet. And the cylinder curve named as wall and symmetry boundary is selected. The half section of the rocket body is selected and named a rocket.

In the pre-processor, a pressure-based solver with steady time is considered. For this analysis, the viscous model with a two-equation K- ω SST model is selected. This shear stress transport turbulence model is preferred for aeronautical applications where adverse pressure changes occur [13]. This solver uses the Reynolds-averaged Navier Stokes (RANS) equation [14] in conservation form [15]. Air is selected as the fluid domain. The magnitude of the inlet velocity varies from Mach number 0.3 to 0.85 with zero-gauge pressure. Zero static pressure is applied to the outlet. Temperature, air density, and viscosity are set to the mean sea level condition. The reference values are taken from the inlet. The rocket boundary is selected with the no-slip condition and the outer wall with the free-slip condition. In the solution methods, coupled scheme and Rhie-chow: distance-based flux type is chosen for the pressure velocity coupling. For the spatial discretization, the least squares cell-based gradient is adapted, and for the pressure, momentum, turbulent kinetic energy, and specific dissipation rate are selected as second-order upwind. The governing equation for the numerical simulation is discussed below [13].

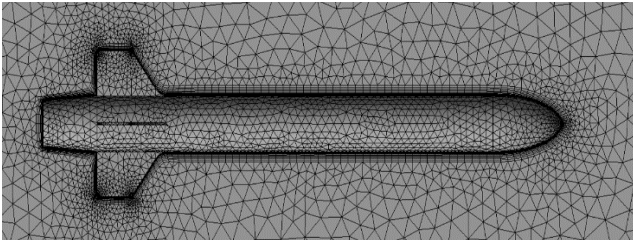


Fig. 2 Rocket body in the meshed fluid domain

The continuity equation:

$$\frac{\partial \rho}{\partial t} + \nabla \cdot (\rho U) = 0, \quad (13)$$

where: ρ is fluid density; U is flow velocity; t is time.

The momentum equations:

$$\frac{\partial (\rho U)}{\partial t} + \nabla \cdot (\rho U \otimes U) = -\nabla p + \nabla \cdot \tau + S_M, \quad (14)$$

where: p is pressure; S_M is the source of the momentum; τ is the stress tensor.

The total energy equation:

$$\begin{aligned} \frac{\partial (\rho h_{tot})}{\partial t} + \nabla \cdot (\rho U h_{tot}) = \\ = \nabla \cdot (\lambda \nabla T) + \nabla \cdot (U \cdot \tau) + U \cdot S_M + S_E, \end{aligned} \quad (15)$$

where: λ is thermal conductivity; S_E is energy source; h_{tot} is total enthalpy velocity vector; T is temperature.

Turbulent kinetic energy k :

$$\begin{aligned} \frac{\partial}{\partial t} (\rho k) + \frac{\partial y}{\partial x_j} (\rho u_j k) = \\ = \rho P - \beta^* \rho \omega k + \frac{\partial}{\partial t} \left[\left(\mu + \sigma^* \frac{\rho k}{\omega} \right) \frac{\partial k}{\partial x_j} \right], \end{aligned} \quad (16)$$

where: ρ is the mass density; k is turbulence kinetic energy; t is the time; P is mean static pressure; σ^* , β^* is the closure coefficients; μ is molecular viscosity; τ is specific Reynolds stress tensor; u_i , u_j is velocity vectors; x_j is the position vector.

Specific rate dissipation ω :

$$\begin{aligned} \frac{\partial}{\partial t} (\rho \omega) + \frac{\partial y}{\partial x_j} (\rho u_j \omega) = \alpha \frac{\omega}{k} P - \beta \rho \omega^2 + \\ + \sigma_d \frac{\rho}{\omega} \frac{\partial k}{\partial x_j} \frac{\partial \omega}{\partial x_j} + \frac{\partial}{\partial x_j} \left[\left(\mu + \sigma \frac{\rho k}{\omega} \right) \frac{\partial \omega}{\partial x_j} \right], \end{aligned} \quad (17)$$

$$p = \tau_{ij} \frac{\partial u_i}{\partial x_j}, \quad (17.1)$$

where: ω is the specific dissipation rate; α , β , σ , σ_d are the closure coefficients; μ is molecular viscosity; τ is the specific Reynolds stress tensor; u_i , u_j is velocity vectors; x_j is the position vector.

4. Comparison and analysis of different nose-shape models

The post-processing result shows the velocity and pressure distribution around the rocket.

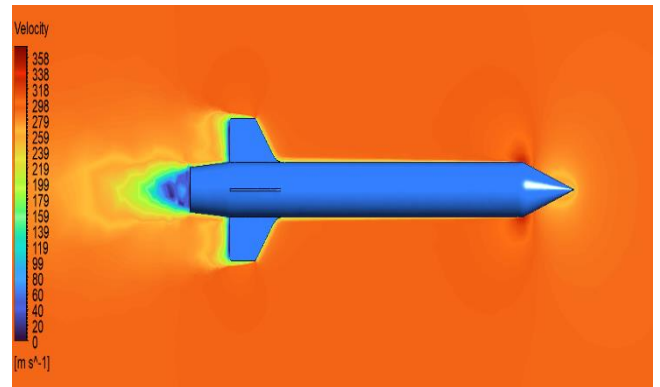


Fig. 3 Velocity contour of rocket with conic nose cone

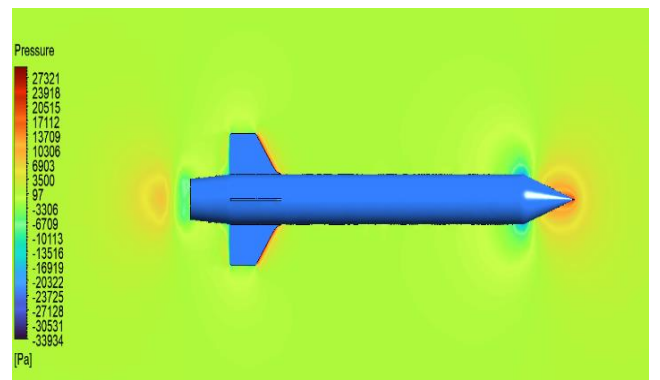


Fig. 4 Pressure distribution of rocket with conic nose shape

The conic geometry shape produces higher drag due to its sharp-edged nose. The lower velocity distribution can be visible near the rear end of the nose cone in Fig. 3. The high concentration of pressure at the tip of the sharp edge as shown in Fig. 4 contributes to the pressure drag and this type of sharp-edged nose cannot be preferred for a subsonic rocket.

The tangent ogive has a lesser drag compared to the conic section as the blunt shape tends to produce lesser drag in the subsonic flow as shown in Fig. 5. As the pressure distribution is lesser compared to the conic. The smooth curvature contributes to the decrement in pressure concentration shown in Fig. 6.

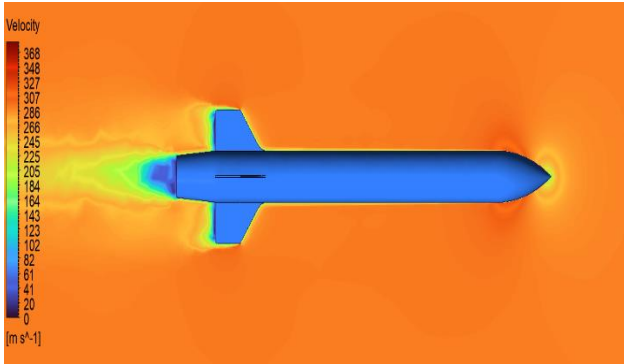


Fig. 5 Velocity distribution of rocket with ogive-nose cone

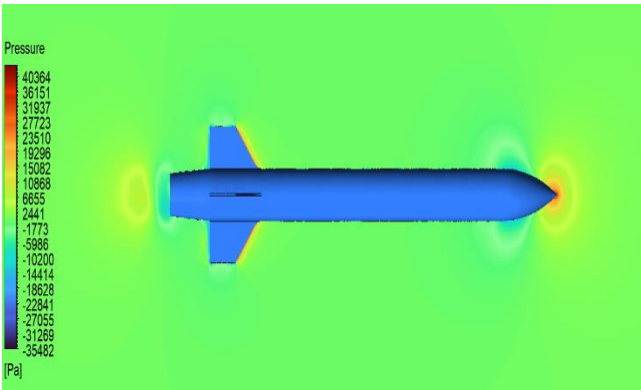


Fig. 6 Pressure contour of rocket with ogive nose

The spherically blunted conic geometry drag variation is like the conic section as the shape has a similarity with the conic except for blunted edge. The velocity distribution is shown in Fig. 7 lesser stagnation pressure near the blunted shape of the cone is visible in Fig. 8.

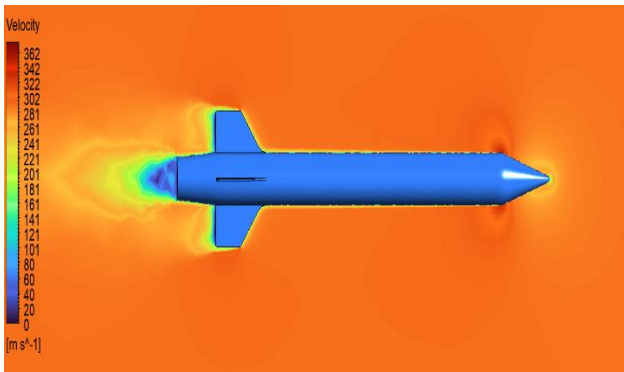


Fig. 7 Velocity contour of rocket with spherically blunted conic nose cone

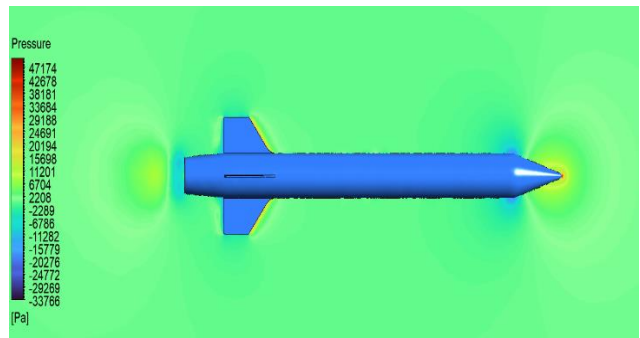


Fig. 8 Pressure contour of rocket with spherically blunted conic nose cone

The bi-conic shape is a segmented cone which with a leading-edge cone is considered smaller compared to the supporting frustum. Therefore, the drag and the coefficient of drag vary considerably lesser than the other profiles. The velocity distribution is shown in Fig. 9 and the pressure distribution is shown in Fig. 10.

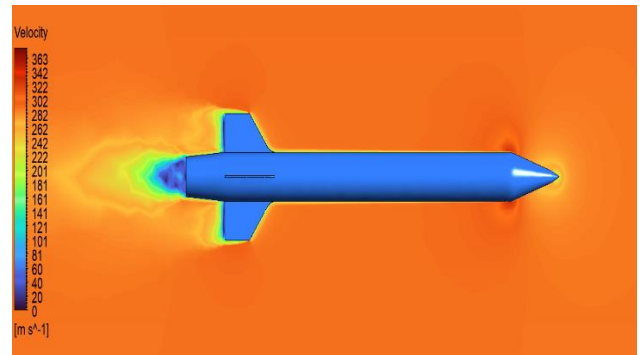


Fig. 9 Velocity distribution of rocket with bi-conic nose

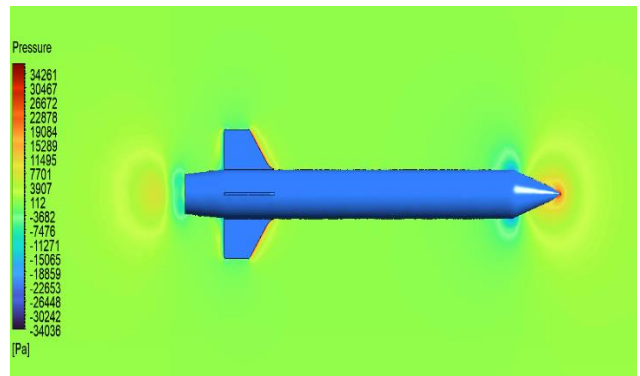


Fig. 10 Pressure distribution of rocket with bi-conic nose

Elliptical geometry produces low drag due to its shape of the blunted nose in the form of an ellipse and fluid flow is smoother and less turbulent compared to the other geometry discussed above as shown in Fig. 7. The stagnation pressure caused the pressure drag is lesser in comparison with other shape discussed before. The pressure contour is shown in Fig. 12.

The parabolic nose geometry gives lesser drag compared to the other geometry selected in this research. Pressure stagnation as shown in Fig. 14 near the tip of the nose contributes to a major part of the pressure drag. The parabolic shape reduces this condition due to its shape and gives a smoother flow and produces lesser turbulence as shown in Fig. 13.

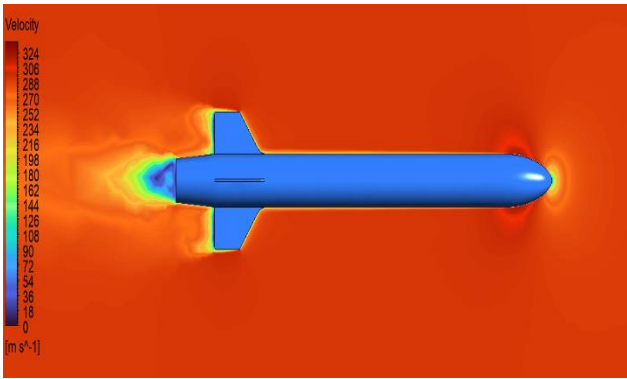


Fig. 11 Velocity contour of rocket with elliptical nose cone

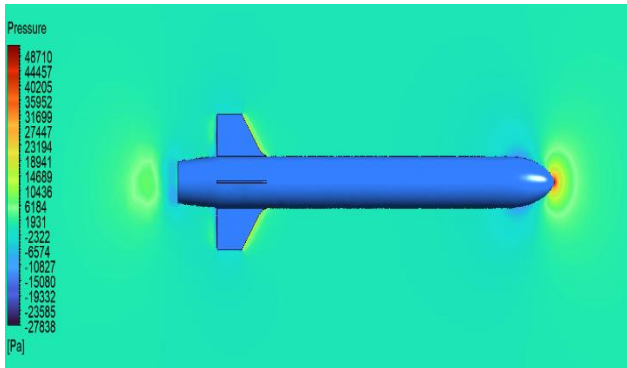


Fig. 12 Pressure contour of rocket with elliptical nose cone

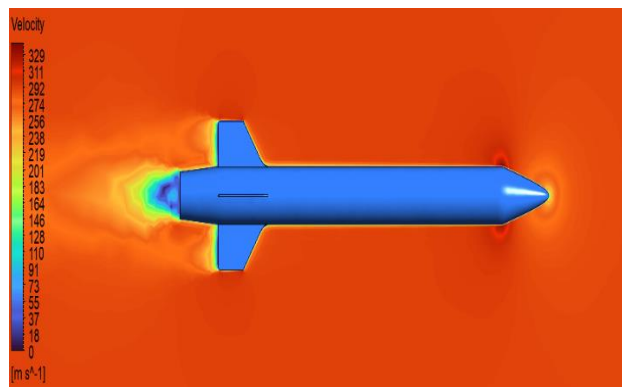


Fig. 13 Velocity contour of rocket with parabolic nose cone

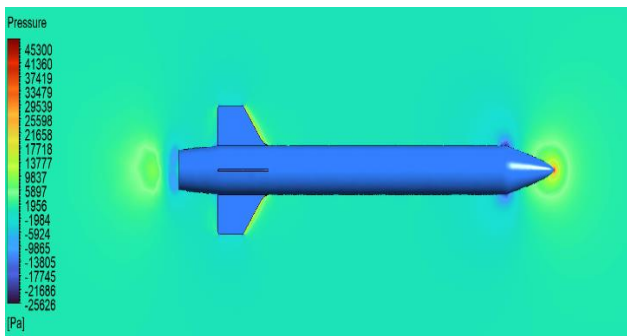


Fig. 14 Pressure contour of rocket with parabolic nose cone

4.1. Drag values plotted for Mach numbers

Drag values of six nose cone shape for Mach number from 0.3 to 0.85 is analysed using computational fluid dynamics analysis. Fig. 15. shows the increase in drag value as the Mach number increases. Similar behaviour is observed for all six nose cones considered. This graph comparison helps to select the less drag shape for the final

model. The drag value depends on the area of the cross-section and the velocity of the object.

$$D = \frac{1}{2} \rho V_t^2 S C_d, \tag{18}$$

where: D is the total drag produced; ρ is fluid density; V_t is terminal velocity; S is the cross-sectional area of the rocket; C_d is the coefficient of drag.

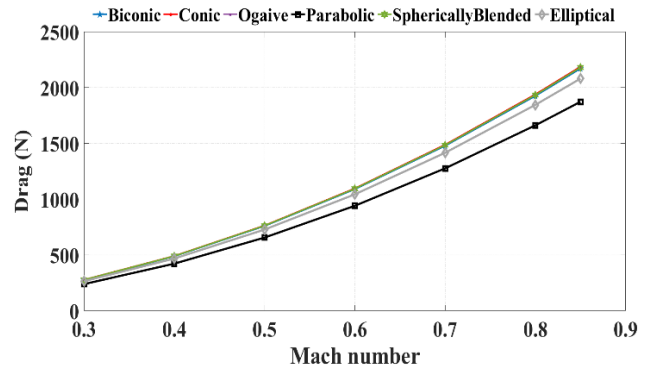


Fig. 15 Drag forces obtained for various Mach number

4.2. Coefficient of drag for six nose cone shapes

Fig. 16 gives a comparison of the coefficient of drag of selected nose cone geometry for various Mach numbers. The C_d vs Mach number graph suggests that the parabolic nose shape has a lesser coefficient of drag. So, this shape is adopted for the computational model.

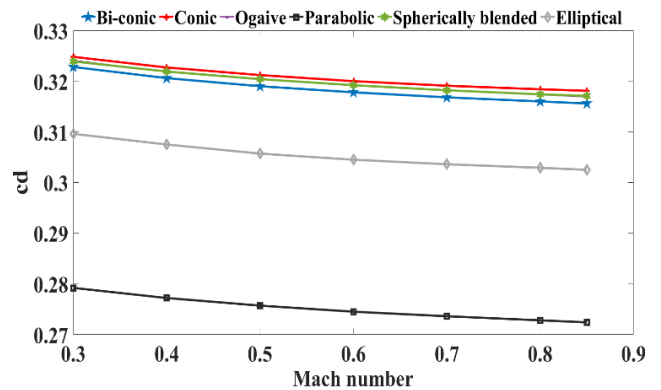


Fig. 16 Six nose cone drag coefficients for various Mach numbers

Fig. 17 gives a computer-aided design model of RT 400M (a) with a parabolic nose cone shape with two RM 12K motors arranged in parallel configuration (b).

5. Results of the ballistic analysis

A total thrust of 24 kN is obtained from the burning of two RM-12K motors simultaneously for 6.2 seconds. Based on the ballistic calculation, the velocity, acceleration versus time graph is obtained. The range and altitude are calculated for various launch angles.

The neutral thrust from the star-shaped solid propellant grain provides the constant thrust for 6.2 seconds. Star-shaped grain is considered for uniform decrement of mass which is helpful for the stability of the rocket. Table 1 gives the basic specification of the rocket target RT-400M.

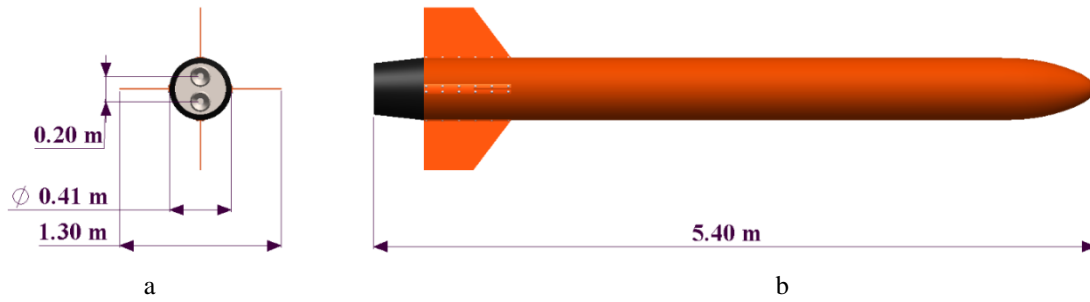


Fig. 17 a) Side; b) Back view of the rocket with two motors

Table 1

Specification of RT-400M

| | |
|---------------------------|-----------|
| Length | 5.4 m |
| Diameter of the body tube | 0.41 m |
| Total motor weight | 72.5 kg |
| Frame mass | 126.05 kg |
| Total mass | 198.05 kg |
| Thrust | 24 kN |
| Burn time | 3.25 s |

5.1. Thrust values of two RM-12K motors plotted against time in seconds

Fig. 18 represents the total thrust force produced by the two solid-fuelled rocket motors. These values are obtained from the experimental static fire test [16].

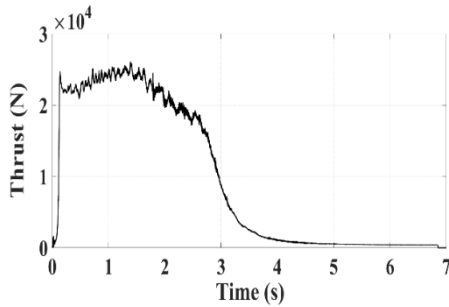


Fig. 18 Thrust vs. Time graph of two RM-12K motors

5.2. Velocity reached by a rocket for various launch angles

$$V_t = \sqrt{\frac{2mg}{\rho ACd}}, \tag{19}$$

where: m is the mass of the rocket; and g is the acceleration due to gravity.

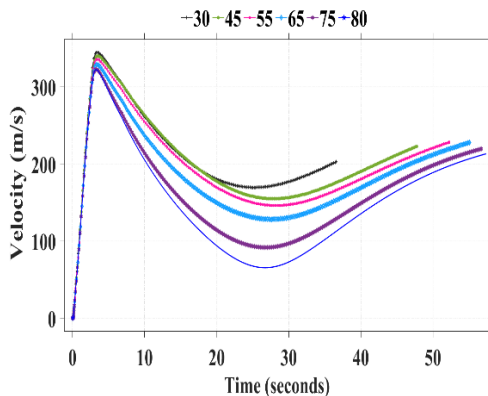


Fig. 19 velocities for different phases of flight

During the active phase of powered flight and the passive phase of unpowered flight profile, the rocket undergoes various velocity values as shown in Fig. 15 from the initial velocity of 0 to the maximum velocity of 330 m/s. for 6.2 seconds on the powered flight, velocity reaches a maximum and begins to drop to in passive flight and the during the descent the vertical velocity vector increases until the touch-down as shown in Fig. 19.

5.3. Acceleration of the rocket for various angles of launch

$$a = \frac{V_0 - V_t \tan \frac{gt}{V_t}}{V_0 + V_t \tan \frac{gt}{V_t}}, \tag{20}$$

where: V_0 is the initial vertical velocity; and t is the time of the flight.

As the velocity varies throughout the flight, the acceleration also varies during the active phase of the flight from 0 to 140 m/s^2 .

There is a slight variation in acceleration for different launch angles. During the active flight phase, the rocket reaches maximum acceleration and during the unpowered phase, the rocket moves only due to acceleration due to gravity as seen in the graph after 6.2 seconds the value increases and then reaches the lowest acceleration as shown in Fig. 20.

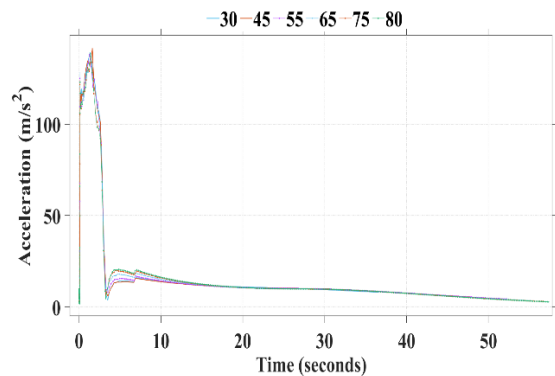


Fig. 20 Acceleration for different flight phases

5.4. Distance of the rocket reached for different angles of launch

$$x = \frac{V_t^2}{g} \ln \left(\frac{(V_t^2 + gV_t t)}{V_t^2} \right), \tag{21}$$

where V_i is the initial horizontal velocity.

Based on the amount of thrust obtained from the burning of two motors and the CFD analysis for drag and c_d the distance in kilometres to be obtained is calculated and shown in Fig. 21. Distance of the rocket is determined by the horizontal component of the velocity vector. A steeper angle has lesser values to the horizontal component and reaches a lesser distance. And at 45 to 60 degrees of launch vertical and horizontal component is equal and makes the rocket reach the furthest distance.

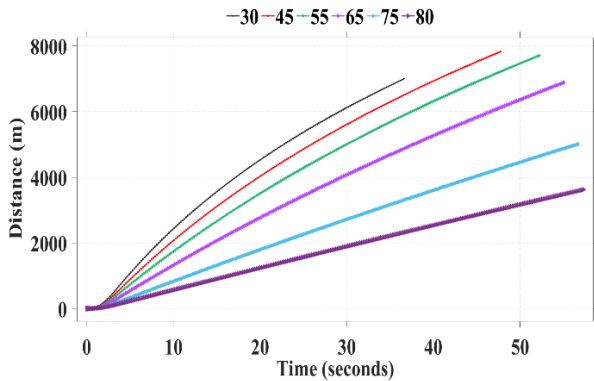


Fig. 21 Distance reached for different angles of launch

5.5. Altitudes reached for various launch angles

$$y = \frac{V_r^2}{2.g} \ln \left(\frac{V_0^2 + V_r^2}{V_i^2} \right). \quad (22)$$

Fig. 22 represents the various altitudes reached by the rocket for different launch angles. At the steeper launch angle, the vertical velocity component helps the rocket reach

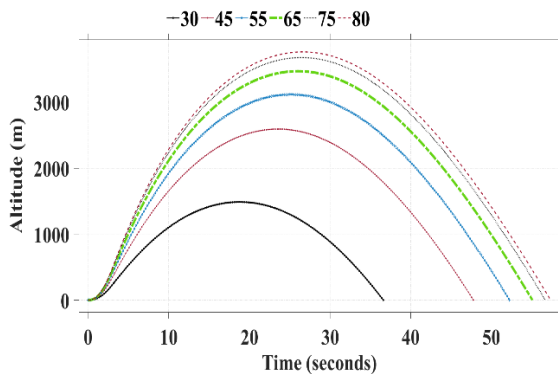


Fig. 22 altitudes reached for different launch angles

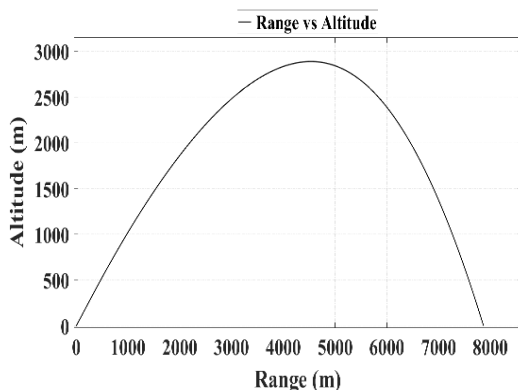


Fig. 23 Maximum rocket range

maximum altitude. At 80 degrees the rocket reaches an altitude of 3750 m. As this rocket is not designed for upper atmospheric study missions, a 90-degree launch is not considered. Fig. 23 shows the maximum range of 7800 m reached at 55 degrees of launch angle.

6. Conclusions

Various nose cone shapes were designed computationally to analyse the fluid behaviour over the body to compare the designs for optimum aerodynamic performance.

Finite volume method-based computational fluid dynamic analysis is carried out to analyse the fluid flow around the rocket body.

Based on the numerical simulation results, the parabolic shape provides the least drag and preferred performance for the rocket model. The parabolic nose shape is adopted for the analysis with a coefficient of drag value of 0.29.

The ballistic analysis is performed to calculate the maximum range and altitude of the rocket. The rocket reaches the maximum range of 7800 m launched at an angle of 55 degrees, and the highest altitude of 3750 m is reached at an angle of 80 degrees' launch. The maximum acceleration of 140 m/s^2 is reached. These obtained results will use for the design of the prototype and live fire exercises.

References

1. **Shah, S.; Tanwani, N.; Singh, S. K.; Makwana, M.** 2020. Drag analysis for sounding rocket nose cone, International research journal of engineering and technology [online] IRJET [accessed 24 August 2022]. Available from internet: https://www.academica.edu/44302678/IRJET_Drag_Analysis_for_Sounding_Rocket_Nose_Cone.
2. **Fedaravicius, A.; Kilikevicius, S.; Survila, A.; Patasiene, L.** 2016. Analysis of aerodynamic characteristics of the rocket-target for the „Stinger” system, Problemy mechatroniki: uzbrojenie, lotnictwo, inzynieria bezpieczenstwa 7(1): 7-16. <https://doi.org/10.5604/20815891.1195197>.
3. **Şummu, A.; Guzelbey, İ. H.; Ogucu, O.** 2020. Aerodynamic shape optimization of a missile using a multi-objective genetic algorithm, International journal of aerospace engineering. <https://doi.org/10.1155/2020/1528435>.
4. **Aytac, Z.; Aktas, F.** 2020. Utilization of CFD for the aerodynamic analysis of a subsonic rocket, Journal of polytechnic 23(3): 879-887. <https://doi.org/10.2339/politeknik.711003>.
5. **Srinivas, G.; Prakash, M. V. S.** 2017. Aerodynamics and flow characterisation of multistage rockets, IOP Conference Series: Materials science and engineering 197(1): 12-77. <https://doi.org/10.1088/1757-899X/197/1/012077>.
6. **Gary, A.; Crowell, Sr.** 1996. The descriptive geometry of nose cones. [online] UFPR [accessed 8 July. 2022]. Available from Internet: <https://dokumen.tips/documents/the-descriptive-geometry-of-nose-cone.html>.
7. **Robbins, N.** 2018. Performance of nose cone geometries on sounding rockets [online]. McGill [accessed 24 August 2022]. Available from Internet: <https://escholarship.mcgill.ca/concern/papers/vh53x178k?locale=en>

8. **Mathew, B. C.; Bandyo, O.; Tomar, A.; Kumar, A.; Ahuja, A.; Patil, K.** 2021. A review on computational drag analysis of rocket nose cone, Workshop on control and embedded systems [online] [accessed 7 June 2021]. Available from internet: https://www.researchgate.net/publication/352213667_A_review_on_computational_drag_analysis_of_rocket_nose_cone.
9. **Rein, M.; Rosemann, H.; Schulein, E.** 2009. Wave drag reduction by means of aerospike on transonic wings, *Shock Waves*, p. 1309-1313. https://doi.org/10.1007/978-3-540-85181-3_83.
10. **Rosy, S.; Antony, M. D.; Sreeshin, M.** 2020. Study on various types of nose cone profiles at supersonic speed through analytical, experimental and numerical simulation methods, *Journal of Xidian university* 14(6). <https://doi.org/10.37896/jxu14.6/312>.
11. **Costello, M.; Gatto, S.; Sahu, J.** 2007. Using computational fluid dynamics-rigid body dynamic (CFD-rbd) results to generate aerodynamic models for projectile flight simulation, proceedings of the institution of mechanical engineers part g journal of aerospace engineering, Proceedings of the institution of mechanical engineers part g journal of aerospace engineering. <https://doi.org/10.1243/09544100JAERO304>.
12. **Ito, Y.; Nakahashi, K.** 2004. Improvements in the reliability and quality of unstructured hybrid mesh generation, *International journal for numerical methods in fluids* 45(2): 79-108. <https://doi.org/10.1002/flid.669>.
13. **Tu, J.; Yeoh, G.; Liu, C.** 2018. Governing equations for CFD: fundamentals, computational fluid dynamics, 65-124. <https://doi.org/10.1016/B978-0-08-101127-0.00003-9>.
14. Navier-Stokes equations. [online]. CFD online [accessed 15 February 2022]. Available from internet: https://www.cfd-online.com/Wiki/Navier-Stokes_equations.
15. **Lauder, B. E.; Spalding, D. B.** 1974. The numerical computation of turbulent flows, *Computer methods in applied mechanics and engineering* 3(2): 269-289. [https://doi.org/10.1016/0045-7825\(74\)90029-2](https://doi.org/10.1016/0045-7825(74)90029-2).
16. **Rackauskas, S.; Fedaravičius, A.; Survila, A.** 2019. Numerical study on internal ballistics characteristics of a solid propellant rocket motor, *Mechanika* 25(3): 187-196. <https://doi.org/10.5755/j01.mech.25.3.23742>.

H. P. Manimaran, A. Fedaravičius

COMPARISON OF NOSE CONE SHAPES AND EXTERNAL BALLISTIC ANALYSIS OF A ROCKET TARGET WITH TWO MOTORS IN A PARALLEL CONFIGURATION

S u m m a r y

In this research, the numerical analysis is conducted to study the aerodynamic characteristics of the rocket target RT-400M with two motors arranged in parallel configuration with different nose cone shapes and performed ballistics analysis on drag values obtained from the finalised nose shape. Two RM 12K motors are used to increase range. This method reduces the R&D cost required to develop the new rocket motor with extended thrust. Reynolds averaged Navier-Stokes equation with $k-\omega$ SST model is adapted for the analysis. A parabolic nose shape produces the least values of drag, drag coefficient, and required velocities. A rocket target with a parabolic nose produces a maximum cd value of 0.29 and is used for the external ballistic calculation. Thrust values of the two motors are obtained from the experimental study. This rocket configuration reaches a maximum of 7800 m distance and a maximum of 3750 m in altitude.

Keywords: Rocket target, ballistics, CFD, nose cone, solid propellant, RANS modelling, finite-volume method.

Received August 23, 2022

Accepted April 5, 2023



This article is an Open Access article distributed under the terms and conditions of the Creative Commons Attribution 4.0 (CC BY 4.0) License (<http://creativecommons.org/licenses/by/4.0/>).